Ultra-fast photoacoustic flow cytometry with a 0.5 MHz pulse repetition rate nanosecond laser

Dmitry A. Nedosekin,[1] Mustafa Sarimollaoglu,[1] Evgeny V. Shashkov,[1,2] Ekaterina I. Galanzha,[1] Vladimir P. Zharov,[1,*]

[1]*Phillips Classic Laser and Nanomedicine Laboratories, University of Arkansas for Medical Sciences, 4301 W. Markham St., Little Rock, AR, 72205, USA*

[2]*Prokhorov General Physics Institute, Moscow 119991, Russia*

**ZharovVladimirP@uams.edu*

Abstract: In vivo photoacoustic (PA) flow cytometry (PAFC) has great potential for detecting disease-associated biomarkers in blood and lymph flow, as well as real-time control of the efficacy of photothermal (PT) and other therapies through the counting of circulating abnormal objects. We report on a high speed PAFC with a Yb-doped fiber laser having a 0.5-MHz pulse repetition rate at a wavelength of 1064 nm, pulse width of 10 ns, and energy up to 100 μJ. This is the first biomedical application of PA and PT techniques operating at the highest pulse repetition rate of nanosecond lasers that provide 100-fold enhancement in detection speed of carbon nanotube clusters, as well as real-time monitoring of the flow velocity of individual targets through the width of PA signals. The laser pulse rate limits for PT and PA techniques depending on the sizes of laser beam and targets and flow velocity are discussed. We propose time-overlapping mode and generation of periodic nano- and microbubbles as PA-signal and PT-therapy amplifiers, including discrimination of small absorbing targets among large ones. Taking into account the relatively low level of background signals from most biotissues at 1064 nm, our data suggest that a nanosecond Yb-doped fiber laser operating at high pulse repetition rate could be a promising optical source for time-resolved PA and PT cytometry, imaging, microscopy, and therapy, including detection of nanoparticles and cells flowing at velocities up to 2.5 m/s.

OCIS codes: (170.0170) Medical optics and biotechnology; (170.1470) Blood or tissue constituent monitoring; (350.5340) Photothermal effects; (170.1530) Cell analysis; (350.4990) Particles.

References and links

1. V. P. Zharov, and V. S. Letokhov, *Laser optoacoustic spectroscopy* (New York: Springer-Verlag, 1986).
2. S. E. Bialkowski, *Photothermal spectroscopy methods for chemical analysis* (A Wiley-Interscience publication, New York, 1996).
3. L. Wang, ed., *Photoacoustic Imaging and Spectroscopy* (Taylor & Francis/CRC Press, 2009).
4. V. P. Zharov, E. I. Galanzha, and V. V. Tuchin, "Photothermal imaging of moving cells in lymph and blood flow in vivo," Proc. SPIE **5320**, 256–263 (2004).
5. V. P. Zharov, E. I. Galanzha, E. V. Shashkov, N. G. Khlebtsov, and V. V. Tuchin, "In vivo photoacoustic flow cytometry for monitoring of circulating single cancer cells and contrast agents," Opt. Lett. **31**(24), 3623–3625 (2006).
6. V. P. Zharov, E. I. Galanzha, E. V. Shashkov, J. W. Kim, N. G. Khlebtsov, and V. V. Tuchin, "Photoacoustic flow cytometry: principle and application for real-time detection of circulating single nanoparticles, pathogens, and contrast dyes in vivo," J. Biomed. Opt. **12**(5), 051503 (2007).
7. E. I. Galanzha, E. V. Shashkov, V. V. Tuchin, and V. P. Zharov, "In vivo multispectral, multiparameter, photoacoustic lymph flow cytometry with natural cell focusing, label-free detection and multicolor nanoparticle probes," Cytometry A **73A**(10), 884–894 (2008).

#122154 - $15.00 USD Received 5 Jan 2010; revised 3 Mar 2010; accepted 29 Mar 2010; published 9 Apr 2010

8. E. I. Galanzha, E. V. Shashkov, P. M. Spring, J. Y. Suen, and V. P. Zharov, "In vivo, noninvasive, label-free detection and eradication of circulating metastatic melanoma cells using two-color photoacoustic flow cytometry with a diode laser," Cancer Res. **69**(20), 7926–7934 (2009).
9. J. W. Kim, E. I. Galanzha, E. V. Shashkov, H. M. Moon, and V. P. Zharov, "Golden carbon nanotubes as multimodal photoacoustic and photothermal high-contrast molecular agents," Nat. Nanotechnol. **4**(10), 688–694 (2009).
10. E. I. Galanzha, E. V. Shashkov, T. Kelly, J.-W. Kim, L. Yang, and V. P. Zharov, "In vivo magnetic enrichment and multiplex photoacoustic detection of circulating tumour cells," Nat. Nanotechnol. **4**(12), 855–860 (2009).
11. E. I. Galanzha, J. W. Kim, and V. P. Zharov, "Nanotechnology-based molecular photoacoustic and photothermal flow cytometry platform for *in vivo* detection and killing circulating cancer stem cells," J. Biophotonics **2**(12), 725–735 (2009).
12. H. P. Brecht, D. S. Prough, Y. Y. Petrov, I. Patrikeev, I. Y. Petrova, D. J. Deyo, I. Cicenaite, and R. O. Esenaliev, "In vivo monitoring of blood oxygenation in large veins with a triple-wavelength optoacoustic system," Opt. Express **15**(24), 16261–16269 (2007).
13. R. M. Weight, J. A. Viator, P. S. Dale, C. W. Caldwell, and A. E. Lisle, "Photoacoustic detection of metastatic melanoma cells in the human circulatory system," Opt. Lett. **31**(20), 2998–3000 (2006).
14. W. He, H. F. Wang, L. C. Hartmann, J. X. Cheng, and P. S. Low, "In vivo quantitation of rare circulating tumor cells by multiphoton intravital flow cytometry," Proc. Natl. Acad. Sci. U.S.A. **104**(28), 11760–11765 (2007).
15. V. P. Zharov, E. I. Galanzha, and V. V. Tuchin, "Photothermal flow cytometry in vitro for detection and imaging of individual moving cells," Cytometry A **71A**(4), 191–206 (2007).
16. E. I. Galanzha, M. S. Kokoska, E. V. Shashkov, J. W. Kim, V. V. Tuchin, and V. P. Zharov, "In vivo fiber-based multicolor photoacoustic detection and photothermal purging of metastasis in sentinel lymph nodes targeted by nanoparticles," J Biophotonics **2**(8-9), 528–539 (2009).
17. I. Y. Petrova, R. O. Esenaliev, Y. Y. Petrov, H. P. E. Brecht, C. H. Svensen, J. Olsson, D. J. Deyo, and D. S. Prough, "Optoacoustic monitoring of blood hemoglobin concentration: a pilot clinical study," Opt. Lett. **30**(13), 1677–1679 (2005).
18. Y. Y. Petrov, D. S. Prough, D. J. D. Deyo, M. M. Klasing, M. Motamedi, and R. O. Esenaliev, "Optoacoustic, noninvasive, real-time, continuous monitoring of cerebral blood oxygenation: an in vivo study in sheep," Anesthesiology **102**(1), 69–75 (2005).
19. I. Y. Petrova, Y. Y. Petrov, R. O. Esenaliev, D. J. Deyo, I. Cicenaite, and D. S. Prough, "Noninvasive monitoring of cerebral blood oxygenation in ovine superior sagittal sinus with novel multi-wavelength optoacoustic system," Opt. Express **17**(9), 7285–7294 (2009).
20. S. H. Holan, and J. A. Viator, "Automated wavelet denoising of photoacoustic signals for circulating melanoma cell detection and burn image reconstruction," Phys. Med. Biol. **53**(227–N), 236 (2008).
21. M. Xu, and L. V. Wang, "Photoacoustic imaging in biomedicine," Rev. Sci. Instrum. **77**(4), 041101 (2006).
22. H. M. Shapiro, *Practical Flow Cytometry* (Wiley-Liss, New York, 2003).
23. D. A. Watson, L. O. Brown, D. R. Gaskill, M. Naivar, S. W. Graves, S. K. Doorn, and J. P. Nolan, "A flow cytometer for the measurement of Raman spectra," Cytometry A **73A**(2), 119–128 (2008).
24. J.-W. Kim, E. V. Shashkov, E. I. Galanzha, N. Kotagiri, and V. P. Zharov, "Photothermal antimicrobial nanotherapy and nanodiagnostics with self-assembling carbon nanotube clusters," Lasers Surg. Med. **39**(7), 622–634 (2007).
25. G. M. Hale, and M. R. Querry, "Optical constants of water in the 200 nm to 200 μm wavelength region," Appl. Opt. **12**(3), 555–563 (1973).
26. W. G. Zijlstra, A. Buursma, and O. W. van Assendelft, *Visible and Near Infrared Absorption Spectra of Human and Animal Haemoglobin* (VSP, Utrecht 2000).
27. V. P. Zharov, R. R. Letfullin, and E. N. Galitovskaya, "Microbubbles-overlapping mode for laser killing of cancer cells with absorbing nanoparticle clusters," J. Phys. D Appl. Phys. **38**(15), 2571–2581 (2005).
28. G. Ku, B. D. Fornage, X. Jin, M. H. Xu, K. K. Hunt, and L. V. Wang, "Thermoacoustic and photoacoustic tomography of thick biological tissues toward breast imaging," Technol. Cancer Res. Treat. **4**(5), 559–566 (2005).
29. H. P. Brecht, R. Su, M. Fronheiser, S. A. Ermilov, A. Conjusteau, and A. A. Oraevsky, "Whole-body three-dimensional optoacoustic tomography system for small animals," J. Biomed. Opt. **14**(6), 064007 (2009).
30. A. N. S. Institute, American National Standard for the Safe Use of Lasers, ANSI Z136.1–2000, (American National Standards Institute, Washington, DC, 2000).
31. R. R. Letfullin, C. Joenathan, T. F. George, and V. P. Zharov, "Laser-induced explosion of gold nanoparticles: potential role for nanophotothermolysis of cancer," Nanomedicine (Lond) **1**(4), 473–480 (2006).
32. H. Fang, K. Maslov, and L. V. Wang, "Photoacoustic Doppler flow measurement in optically scattering media," Appl. Phys. Lett. **91**(26), 264103 (2007).

1. Introduction

Photoacoustic (PA) spectroscopy and imaging demonstrate higher sensitivity and resolution in deeper tissue (up to 3 cm) than other optical modalities including scattering and fluorescent techniques [1–3]. Recently, we introduced photothermal (PT) and PA cytometry using laser-

#122154 - $15.00 USD Received 5 Jan 2010; revised 3 Mar 2010; accepted 29 Mar 2010; published 9 Apr 2010

induced thermal and accompanying acoustic and nanobubble-formation phenomena either in single cells with intrinsic absorption or in strongly absorbing nanoparticles used as PA and PT molecular high-contrast agents [4–11]. The capacity of this clinically relevant technology was demonstrated by the real-time detection in blood and lymph flow of circulating individual normal cells (e.g., erythrocytes and leukocytes) in different functional states (e.g., normal, apoptotic, or necrotic), tumor cells (melanoma, breast, squamous), bacteria (e.g., *E. coli* and *S. aureus*), nanoparticles (e.g., gold nanorods [5], carbon nanotubes [CNTs] [6], magnetic [10,11] and golden carbon nanotubes [9–11]), and dyes (e.g., Lymphazurin, Evans blue, and Indocyanine Green). Compared to other promising approaches (e.g., [3,12–14]), PT and especially PA flow cytometry (PAFC) offers the following advantages: 1) use of low-toxicity nanoparticles approved for a pilot study in humans; 2) high-resolution (300 nm) PT imaging of flowing single cells of interest at velocities up to 2 m/s [15]; 3) PT and PA measurements of the velocity of individual flowing cells [8]; 4) integration of PAFC with simultaneous highly localized PT therapy (e.g., for killing the most aggressive cancer stem cells [8–11]) with PAFC implemented as a diagnostic tool and feedback for real-time control of the efficacy of therapy by counting circulating abnormal objects [8,11]; 5) PA detection of disseminated tumor cells in lymphatics as the earliest prognostic marker of metastasis, compared to sentinel lymph node and blood assessment [16]; 6) use of magnetic nanoparticles as multifunctional PA-PT-magnetic resonance imaging contrast agents for *in vivo* magnet-induced nanoparticle clustering, nanobubble-related signal amplification, imaging, and cell enrichment/sorting/separation [10,11]; 7) the use of PAFC both with non-invasive and minimally-invasive delivery of laser radiation [6, 8]; and 8) laser scanning PT and PA cytometry mode [8,9,16].

Realization of these advantages, as well as many other potential applications, however, requires fast-detection schematics based on a high pulse repetition rate (PRR) laser. This would ensure the absence of false-negative results caused by cells or particles passing the detection volume without being irradiated by a laser pulse. Indeed, at low laser PRRs, some cells or particles could pass the detection window between laser pulses. Currently, the PRRs of the laser sources used in *in vivo* PA techniques are mostly limited to the 10–50 Hz level [3–7, 12, 13, 17–20]. PA tomography of static objects used an ~1-kHz laser [21]. Recently, we demonstrated PAFC with a diode laser operating at 10 kHz at 905 nm [8]; however, its relatively low pulse energy level (a few microjoules) with a pulse width of 15–200 ns may limit its sensitivity for studying low-absorbing or relatively small targets. *In vivo* fluorescence imaging [14] can be used with a quasi continuous wave femtosecond laser that provides repetitive linear scans and can image blood vessels up to a 200-Hz rate. Although sensitive, this approach is limited by the potential toxicity of available fluorescent labels. In this connection, PAFC methods based on light-absorbing endogenous and exogenous contrast are more promising for many applications [1–3]. It should be noted that conventional, commercially available flow cytometers are well established, powerful biological tools with the capability to analyze up to 10^5 cells per second *in vitro* [22]. However, the multicolor laser arrays used in these techniques to detect fluorescence and/or scattered light operate in continuous-wave mode, which is not well applicable to PAFC. Recently developed *in vitro* flow cytometers with the capability to detect Raman spectra may also operate at only a 1-kHz PRR laser [23].

Thus, further progress in the development of PAFC, as well as other PT and PA techniques, both *in vitro* and *in vivo* can be associated with the application of high-PRR lasers. One main advantage of a fast detection mode in *in vivo* PAFC is the possibility of monitoring large and deep blood vessels with high-velocity cell flow up to 5–50 cm/s compared to 5–10 mm/s in small superficial microvessels [14]. This achievement would result in a shorter time (up to a few minutes compared to a few hours) required for examination of nearly the entire blood volume (~5 liters in adults) in order to detect very rare abnormal (e.g., tumor) cells in the body at early disease stage.

#122154 - $15.00 USD Received 5 Jan 2010; revised 3 Mar 2010; accepted 29 Mar 2010; published 9 Apr 2010

The goal of this work is to explore the opportunity to use a nanosecond laser with high PRRs to improve PAFC`s speed capability. As a first step to verify this approach, we selected the well established and commercially available Yb-doped fiber laser with PRRs up to 500 kHz at 1064 nm. We also answered the following two questions: 1) what are the features of PA signal generation and detection when the temporal interval between successive laser pulses is comparable to the thermal relaxation time of absorbing targets and the duration of the PA signals; and 2) what is the diagnostic value of *in vivo* PAFC at 1064 nm. We selected CNTs as promising PA and PT agents with high PT and PA contrast in the near-infrared spectral region. CNTs were used as the simplest cell, nano- and microparticles phantom in glass tubes flow module [15] for the *in vitro* study, and in nude mice used as the animal model for the *in vivo* study.

2. Material and Methods

2.1 PA flow cytometer

The integrated setup was built as described previously [5–11, 16] on the technical platform of an Olympus BX51 microscope (Olympus America, Inc.) and a tunable optical parametric oscillator (OPO, Lotis Ltd., Minsk, Belarus) with a pulse of 8 ns in width, a repetition rate of 10 Hz, a wavelength in the range of 420–2,300 nm, and a fluence range, $1–10^4$ mJ/cm^2 per pulse [Fig. 1(a)]. To improve PAFC speed, the setup was equipped with near-infrared fiber-based pulsed laser, model MOPA-M-10 (MultiWave Photonics, SA, Portugal) with the fixed wavelength of 1064 nm, pulse width 10 ns, and pulse energy up to 100 μJ. The PRR (further also denoted as f_{rep}) varied from a single shot to 500 kHz. Delivery of laser radiation to blood was performed either with a conventional microscope condenser varying the diameter of the laser beam in the range from 5 to 150 μm, or adding customized cylindrical lens providing linear laser beam with dimensions from 10×50 μm to 25×100 μm, or the use of 330-μm a fiber [Fig. 1(b)]. Energy meter (PE10-SH, OPHIR, Israel) was used to control laser pulse energy. CCD camera Cohu 2122 (Cohu Inc., San Diego, California) was used to navigate laser beams on the samples.

Laser-induced PA waves were detected by an ultrasound transducer (model 6528101, 3.5 MHz, 4.5 mm in diameter; Imasonic Inc., Besançon, France), which was gently attached to animal skin [Fig. 1(b)] or to the upper coverslip of a 120-μm-thick glass slide [Fig. 1(c), 1(d)]. Typical distance from laser spot to transducer was 4-6 mm. To improve reproducibility of transducer readings for all *in vitro* and *in vivo* tests, it was placed flat on the slide and ear [Fig. 1(e)] without fine tuning of transducer orientation. The warmed water or conventional ultrasound gel were topically applied for better acoustic matching between the transducer and the samples. The signals from transducer were amplified (preamplifier model 5662B; bandwidth, 50 kHz – 5 MHz; gain 54 dB; Panametrics NDT, USA) and recorded by a Tektronix TDS-3000B oscilloscope (Tektronix, Inc., USA), and PC (Dell Precision 690). The latter was equipped with a high-speed (200 MHz) analog-to-digital converter board PCI-5152, 12-bit card, 128 MB of memory (National Instruments Inc., USA), in-home written software (based on LabVIEW 8.5; National Instruments Inc., USA). The setup was synchronized with the signal from the laser-radiation-detecting photodiode. The digitizer board was able to acquire the data after consecutive laser pulses at PRRs up to 24 kHz in the on-line mode with real-time data processing. For higher PRRs, the board acquired data for a limited time by filling the data buffer or processing the data off-line using oscilloscope modes.

PT thermal-lens effect was assessed by recording intensity changes in the center of stabilized cw He-Ne laser beam coaxial to excitation beam (wavelength 633 nm, power 1.4 mW, frequency stabilized mode, model 117A, Spectra –Physics Inc., USA) by photodetector with built-in signal amplification (PDA36A, 40 dB amplification, ThorLabs Inc., USA). Full description and methodology of the setup is presented elsewhere [7,8]. PT signals were displayed on the oscilloscope for the analysis of signal shape. Stationary PT thermal-lens

#122154 - $15.00 USD Received 5 Jan 2010; revised 3 Mar 2010; accepted 29 Mar 2010; published 9 Apr 2010

signal was acquired by monitoring probe beam intensity in DC mode. Time- resolved PT thermal-lens signal is acquired in AC oscilloscope mode.

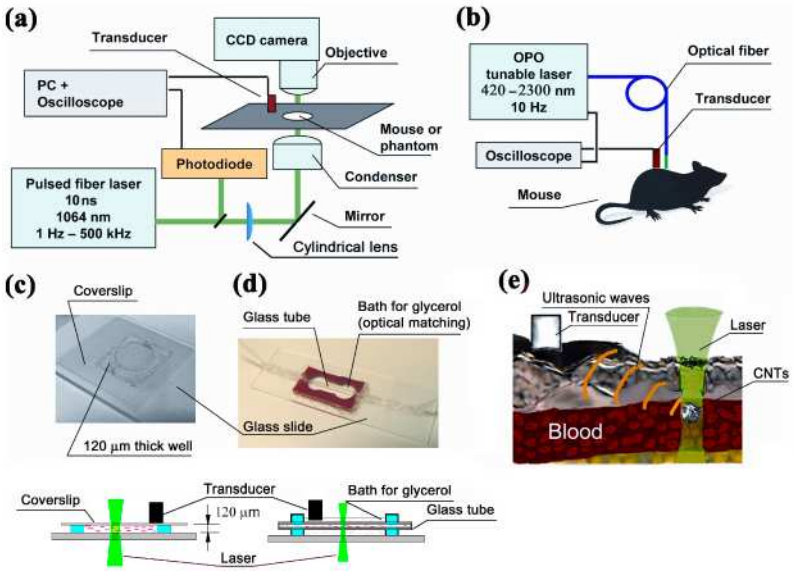

Fig. 1. PAFC. (a) Scheme of the microscope for *in vitro* and *in vivo* studies; (b) fiber delivery of laser radiation; (c) study of CNTs suspension in 120-μm slide; (d) 300-μm glass tube in glycerol bath; (e) *in vivo* PA detection of circulating CNTs.

2.2 Flow module

In vitro flow was realized with a 5 mL syringe pump–driven system (model 780210; KD Scientific Inc.) [Fig. 1(d)] and customized glass tubes (PYREX Disposable Micro-Sampling Pipets, 10 μl, Corning, USA): one with a circular cross-section and inner diameter of 350 μm and the other with a rectangular (50 × 50 μm) cross-section. To minimize optical distortion, glass tubes were immersed in a 99% glycerol solution (Sigma-Aldrich) with a high refractive index. The transducer was attached to glass tube or placed directly into glycerol bath. The syringe and glass tube were connected by 20 cm long silicon tube. This system provided a linear flow velocity in the range of 0.1 mm/s to 2.5 m/s. The average flow velocity was estimated from the collected fluid volume and the known diameter of the tube. The velocity of single particles in flow was measured by frame-by-frame video-recording. In most experiments, we used a phosphate-buffered saline (PBS) solution to prepare nanoparticles suspension.

2.3 Nanoparticles

CNTs with an average length and diameter of 190 nm and 1.7 nm, respectively, were purchased from Carbon Nanotechnologies, Inc. (Houston, TX) and processed as described previously [24]. The solution with CNTs was treated for at least 15 min with an ultrasonic dismembrator to provide uniform distribution of CNT aggregates. The average size of large aggregates in the solution was controlled by optical imaging (100× magnification, Olympus BX51 microscope). Nanoparticle suspension consisted of both individual CNTs and CNT aggregates. Depending on duration of treatment with ultrasound and filtering, the aggregate size can be selected in the broad range of 0.3 nm–25 μm. Light absorption spectrum in the 500–1100 nm range for a 0.1 mg/mL CNT solution was measured with the Ultrospec 3300 pro (Amersham Biosciences, Ltd., UK) spectrophotometer in a 1-cm cuvette.

#122154 - $15.00 USD Received 5 Jan 2010; revised 3 Mar 2010; accepted 29 Mar 2010; published 9 Apr 2010

2.4 Animal model

Nude mice weighing 20–25 g (Harlan Sprague–Dawley) were used in accordance with protocols approved by University of Arkansas for Medical Sciences Institutional Animal Care and Use Committee. Mice were anesthetized with ketamine/xylazine, 50/10 mg/kg, i.p., and placed on a heated microscope stage with an ear spread flat over the glass slide. The transducer was gently attached to the ear to avoid blood vessel squeezing. Typical distance from the laser beam to the transducer was 4–6 mm, which corresponds to a 2–4-μs delay in the arrival of the acoustic waves to the transducer [Fig. 1(e)]. PA spectroscopy was performed on relatively large blood vessels (150–300 μm in diameter) using skin-fold mouse model [8]. Optical fiber delivering laser irradiation was tightly pressed to skin. The transducer was placed at a 12-mm distance from the fiber.

2.5 PA spectroscopy

The PA spectra of the skin and of the skin with blood vessels were obtained by exposure of the skin area of interest to radiation from a tunable OPO delivered by a 330-μm fiber [Fig. 1(b)]. The PA spectrum from skin was recorded in the 850–1100-nm wavelength region [25,26] by tuning the OPO laser without changing the position of the transducer or optical fiber. The averaging of 64 acoustic waves in oscilloscope mode with normalization on the pulse energy was performed to increase the accuracy of the spectroscopic data. The skin area to be irradiated was first selected visually. Large blood vessels in mouse abdominal skin are well distinguishable; the fiber position was finely adjusted to obtain the maximal signal from this blood vessel. The PA spectrum from skin was acquired by positioning the fiber on skin without visible blood vessels.

2.6 PA data analysis

Figure 2(a), 2(b) shows signal diagrams corresponding to the laser pulses (a), and the generation of successive PT signals and bubbles [Fig. 2(b)], and acoustic waves [Fig. 2(c)] from CNTs. The typical duration of PT signals depends on media properties, amount of heat generated and laser spot and sample size (e.g., 30-40 μs for 10-20 μs laser spot and water solution). The PA signals from CNTs initially had a bipolar shape that is transformed into a pulse train with a typical duration of 5–15 μs due to resonance and reflection effects on the transducer–skin-holder interface and in the glass slide. Although not quite optimal, this schematic *in vitro* provides detectable signals from small individual CNT aggregates of 300 nm and larger. The digitizer board acquired these long acoustic waves after the laser pulse. Electronic noise and acoustic oscillations caused by electromagnetic interference and scattered laser light were removed by time-resolved gating. In-house-written LabView-based software digitally filtered each recorded acoustic wave with the use of a bandpass filter setup to pass only oscillations in the range of 750 kHz to 4.5 MHz. This removed the remaining electronic and low-frequency-vibration noise. The resulting peak-to-peak amplitude of PA oscillations was considered as a desired PA signal corresponding to the sample response to the laser pulse [Fig. 2(c)]. For each laser pulse, software processed the acoustic waves, measured PA signal amplitude, and saved the corresponding pulse number and amplitude of the PA signals to the hard drive [Fig. 2(d)]. After calculation of the PA signal amplitude, acoustic wave data was discarded to maximize the performance of the digitizer. The resulting data set for each PAFC experiment included values of PA signal amplitude corresponding to each of successive laser pulses.

The data sets from the PAFC experiment [Fig. 2(d)] were analyzed off-line to find PA signals above the background level by MATLAB 7.7 (Mathworks Inc.) based software written in-house. The software applied 3σ-criterion (triple standard deviation criterion) to distinguish between random fluctuations of signal amplitudes and statistically significant changes. For each individual peak, the following parameters were calculated with the use of

#122154 - $15.00 USD Received 5 Jan 2010; revised 3 Mar 2010; accepted 29 Mar 2010; published 9 Apr 2010

standard and customized MATLAB functions [Fig. 2(d)]: peak position in time (laser pulse number), peak width (number of laser pulses with signal exceeding the triple value of the standard deviation of background signal), peak amplitude (difference between maximal PA signal amplitude and the level of blood background signal amplitude).

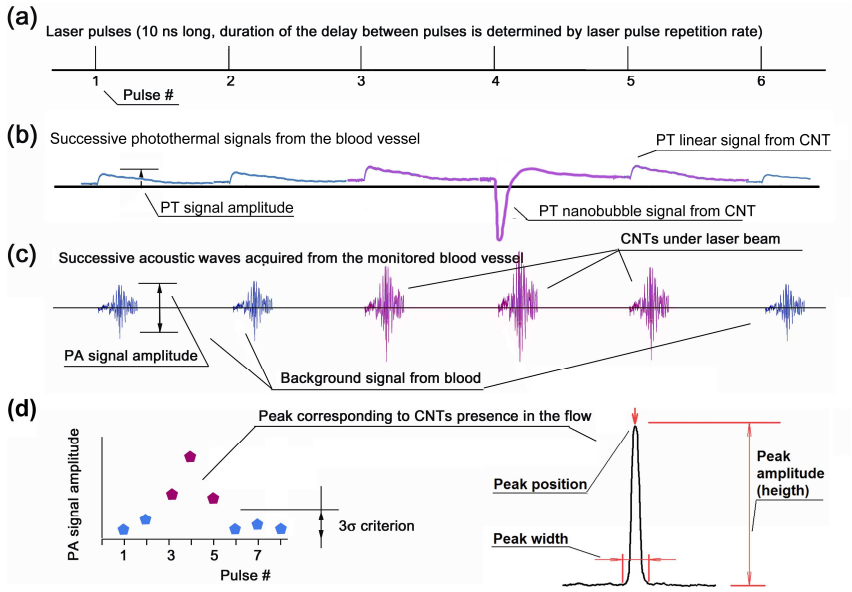

Fig. 2. Signal diagrams: (a) Time diagram of laser pulses; (b) successive PT thermal-lens signals (linear and nanobubbles related signals); (c) laser-induced acoustic waves. Blue signals (# 1, 2, and 5) are background signals from blood and red signals (# 3–5) are from samples in flow with higher local light absorption (CNTs); (d) resulting curve in coordinates of PA signal amplitude vs. pulse number (or time) and curve parameters used to characterize CNTs parameters.

3. Results

3.1 PA effects at a high pulse repetition rate

Generation of PA waves upon absorption of laser radiation at 1064 nm in a broad range of f_{rep} from 1 kHz to 500 kHz was tested *in vitro* in a CNT solution in a 120-μm-thick slide [Fig. 1(c)]. The pulse energy was in the range of 0.1–2 μJ, and the beam was defocused to a diameter up to 150 μm to avoid overheating of the sample. The energy fluence levels were approximately in the range of 0.5–10 mJ/cm^2. For all the PRRs used, pulse energy was constant: thus the average radiation power increased with the increase in repetition rate. The small CNT aggregates (~1 μm) were loosely distributed in the solution to provide efficient heat diffusion from the heated CNTs into the coupling medium. Data recording for different f_{rep} was initiated after 20 s long exposure of the sample to laser irradiation to allow heat generation–dissipation equilibrium to be established. To verify the presence of nano- or microbubbles, we additionally studied PT thermal-lens effects from CNTs. Pulsed thermal-lens response revealed the sample's response to each laser pulse, while stationary thermal-lens was blooming in solution due to heat accumulation. These effects cover a time scale from several microseconds for pulsed time-resolved thermal-lens to seconds for stationary thermal-lens.

At a high pulse energy level (2 μJ), PA signal amplitude dramatically increased with PRR increasing from 1 kHz to 50 kHz [Fig. 3(a)]. This nonlinear signal amplification could be associated with laser-induced bubble formation around overheated CNT clusters with their further overlapping [10, 11, 16, 27]. Bubble formation was verified by the characteristic

#122154 - $15.00 USD Received 5 Jan 2010; revised 3 Mar 2010; accepted 29 Mar 2010; published 9 Apr 2010

shape of the time-resolved pulsed PT thermal-lens signal [Fig. 3(b), curve marked "2.0 μJ; 30 kHz"] (see methodology in [24, 27]). Thus, heat accumulation and especially spatial and partly temporal bubble overlapping (with 1–5 μs in time duration and periodic cavitations of large bubbles) from successive laser pulses may significantly (in our study up to 10–50 times) enhance bubble generation as PT and PA signal amplifiers [8, 10, 24, 27]. At higher PRRs >50 kHz, we even observed formation of air bubbles in the laser beam [Fig. 3(b), curve marked "2.0 μJ; 100 kHz"]. These effects were absent in linear mode at lower laser pulse energy levels in the range of 0.1–1 μJ, when only slight signal variations were observed at different f_{rep} values [Fig. 3(a)]. Analysis of stationary thermal-lens in solution proves that there is heat generation–dissipation equilibrium in the case of linear PA mode resulting in formation of a stationary thermal-lens in solution [Fig. 3(b), curve marked "1.0 μJ"). In nonlinear mode at a high f_{rep} value, solution overheating leads to the emergence of microbubbles [Fig. 3(b), curve marked "1.0 μJ; 100 kHz"].

At PRRs of 100 kHz and higher, PA signals overlapped as a result of the short intervals between successive pulses (e.g., 5 μs for f_{rep} ~200 kHz); PA signal duration was at least 10 μs. In this time-overlapping mode, we observed at least 2-fold resonance amplification of PA signal amplitude at 420 kHz compared to 400 kHz and 450 kHz. The range of frequencies corresponding to amplification of the signal was rather narrow, ~0.2 kHz wide. Depending on experimental configuration, the exact resonance laser repetition rate was in the 410–430-kHz range with 2–4-fold amplification. These effects could be caused by superposition of two and potentially more acoustic waves if the time gap between the two successive laser pulses was shorter than several periods of relatively stable oscillation in PA acoustic waves. As a result, during the stable-phase portions, oscillations with positive amplitudes from both PA signals were summed (Fig. 3d, 400 kHz, bottom right graph).

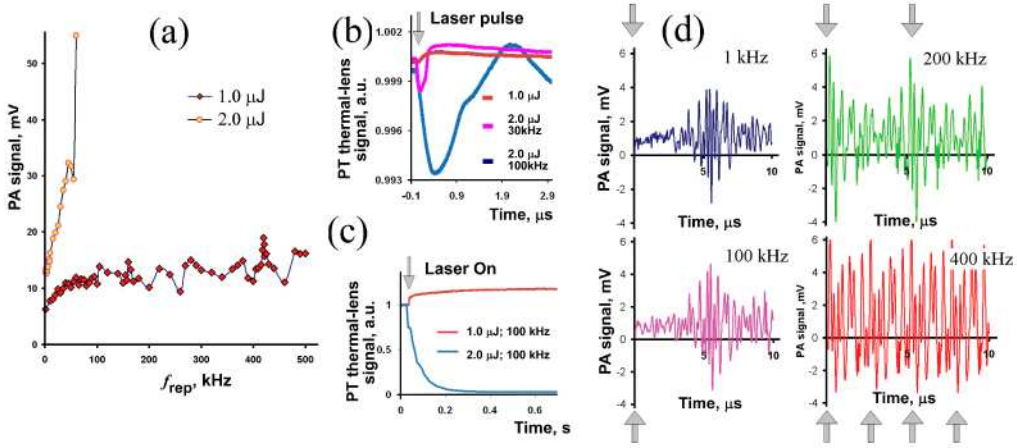

Fig. 3. PA signals from a CNT solution *in vitro*, static conditions: (a) PA signal amplitudes at different f_{rep} for l.0 and 2.0 μJ laser pulse energy, laser spot 150 μm; (b) time-resolved PT thermal-lens signals after a single laser pulse (exact position of the laser pulse is denoted by arrow); (c) PT stationary thermal-lens signals at high f_{rep} values after beginning of excitation (denoted by arrow); (d) PA signal shapes recorded by PAFC in oscilloscope mode for 1, 100, 200, and 400 kHz; laser pulse energy, 1 μJ. Arrows indicate laser pulse position.

3.2 Detection of nanoparticles in mouse blood in vitro

To estimate PA contrast between CNTs and biologically relevant samples at high f_{rep}, we measured PA signals amplitude as a function of the laser fluence from mouse blood alone in 120-μm-thick slides and then from blood with incorporated small, ~3-μm, CNT clusters. Signals from CNTs were acquired by scanning sample with laser beam; transmission optical microscopy was used to verify presence of CNTs. Figure 4 shows the linear behavior of the

#122154 - $15.00 USD Received 5 Jan 2010; revised 3 Mar 2010; accepted 29 Mar 2010; published 9 Apr 2010

PA signal amplitude. The amplitudes of observed PA signals from CNTs were significantly higher than background signals from blood; estimated signal-to-background noise ratio was at least 4.

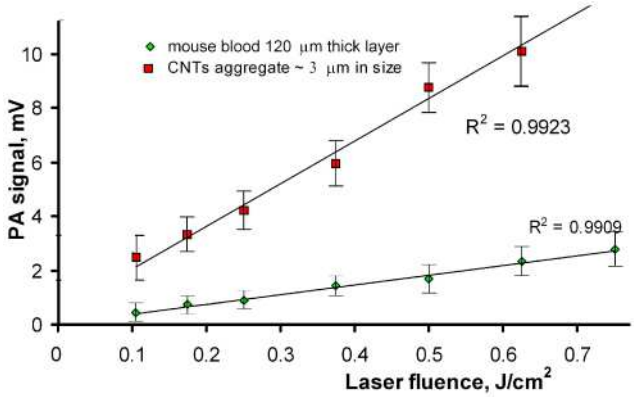

Fig. 4. Amplitudes of PA signals from mouse blood and 3 μm CNT aggregates in 120-μm slide, f_{rep} ~10 kHz, laser spot 25 μm, laser pulse energy 0.5 μJ.

Thus, linear PA signals at 1064 nm were not affected by the laser energy level or the PRRs in specific ranges, and the PA technique may permit detection of small CNT clusters in a 120-μm blood layer and hence in blood vessels with a similar size.

3.3 Testing the capability of PAFC to detect fast moving CNTs in vitro

To estimate the capability of PAFC with a high-PRR laser under flow conditions, a solution containing 15–25-μm CNT aggregates in the glass tube of the flow module was irradiated by adjustment of the low laser pulse energy to produce detectable PA signals only from the aggregates (as rough cell phantoms) and not from individual, non-aggregated CNTs. To avoid missing nanoparticles traveling in different tube cross-sections, the laser beam was transformed by a cylindrical lens into 10×50-μm strip overlapping the entire 50-μm cross-section.

Figure 5(a) shows the PA signal traces (i.e., signal amplitudes distribution in time) from flowing CNTs at different concentrations. Each peak indicates one individual CNT cluster crossing the laser beam and irradiated with at least 10–20 laser pulses. Nevertheless, there is the probability, especially at a high CNT concentration, of simultaneously detecting a few CNT clusters in the laser beam [Fig. 5(a), top]. Use of a diluted solution of CNTs (5 μg/mL), along with the use of a small (50 μm) tube, provided the conditions for detecting individual nanoclusters [Fig. 5(a), middle]. Further dilution of the CNT solution led to a decrease in the number of observed peaks [Fig. 5(a), bottom]. The peak count (i.e., number of CNT aggregates) was based on the triple standard deviation criterion used to distinguish between background signal fluctuations and a statistically significant increase in PA signals. We found a good correlation between the number of observed peaks and the extent of solution dilution [Fig. 5(b)]. In the control experiment using pure deionized water, no peaks were detected. The width of each peak is expected to equal the number of laser pulses that were able to expose the same CNT cluster. To check this, we compared peak widths recorded at different PRRs of the excitation laser. To consider only nanoparticles with similar sizes, the peaks in a narrow amplitude range were selected for comparison. The resulting average peak widths calculated from these data linearly depended on the laser f_{rep} [Fig. 5(c)]. Thus, at a higher rate there are more laser pulses that could irradiate nanoparticles in the solution as they passed through the detection volume. With the known linear flow rate of the solution (3.4 cm/s) and the given peak widths' dependence on the laser pulse, one can calculate nanoparticle lifetime in the detection volume. For example the slope value at Fig. 5(c) is 0.6×10^{-3} s; so a nanoparticle is

#122154 - $15.00 USD Received 5 Jan 2010; revised 3 Mar 2010; accepted 29 Mar 2010; published 9 Apr 2010

in the beam for 0.6 ms. This value corresponds to the 20-µm distance that the solution travels in the capillary and is close both to the average size of the particles in solution and to the laser beam size as was determined by optical imaging.

The performance of PAFC was also tested in a large, 350-µm-diameter tube with higher linear flow velocity up to 2.5 m/s at a flow rate of 800 mL/h. At this flow velocity, a 20-µm nanoparticle passes the 50-µm-wide detection zone in 60 µs. Under this condition, PAFC operating at f_{rep} <17 kHz would not detect the nanoparticle if it passed between successive laser pulses. A comparison of the signals recorded at 9 kHz and 24 kHz for a 2.5 m/s flow velocity is shown in Fig. 6. The experimental data demonstrate that at higher PRRs, more nanoparticles were recorded for the same volume of solution pumped (53 peaks at 24 kHz compared to 35 peaks at 9 kHz for 1-s-long experiments). CNT-aggregate counts at different flow velocities are in a good agreement with the expected decrease in aggregate numbers observed at a lower flow rate, when a smaller volume of test solution was pumped through the detection zone. At a 1 m/s flow rate, there were ~2-fold fewer peaks detected than at 2.5 m/s. This demonstrates that at high laser PRR, there is a higher chance of detecting every single target in flow. Thus, PAFC with a high-PRR laser provides successful detection of CNTs aggregates in extremely fast flows with linear flow velocity up to 2.5 m/s.

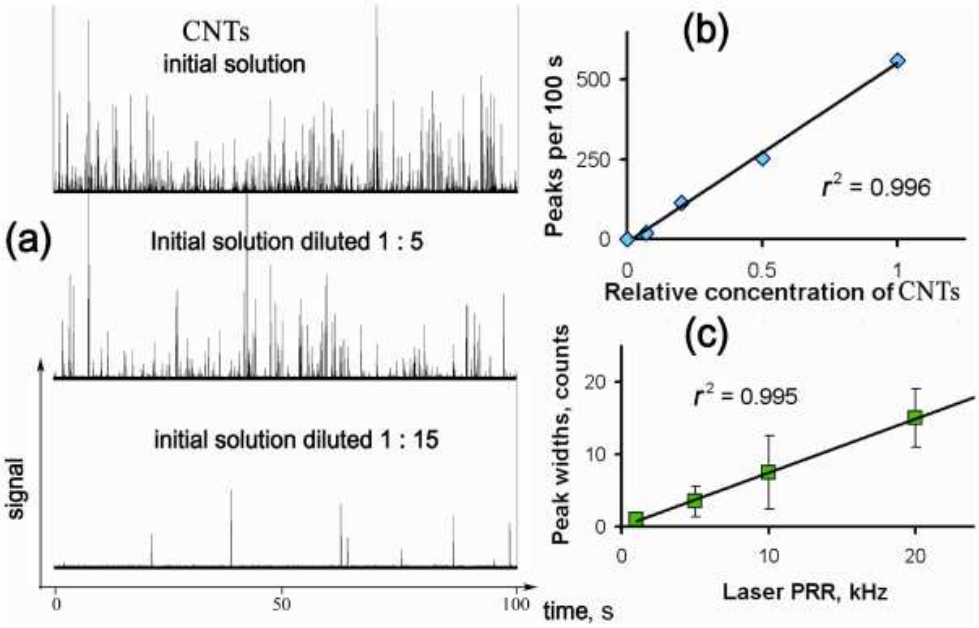

Fig. 5. PA detection of CNTs flowing in a 50-µm tube *in vitro*. (a) Traces of PA signals at the initial concentration of CNTs of 5 µg/mL and at different dilutions. The duration of displayed data is 100 s, and f_{rep} = 10 kHz; (b) calibration graph for different CNT solutions based on data presented in part a; (c) average peak widths with the highest signal amplitudes as a function of the laser PRR. The intervals shown are confidence intervals for each data point n=20, *P*=0.95. Conditions of all experiments: flow rate, 3.4 cm/s; laser pulse energy, 1.5 µJ; laser beam size area, 10×50 µm.

#122154 - $15.00 USD Received 5 Jan 2010; revised 3 Mar 2010; accepted 29 Mar 2010; published 9 Apr 2010

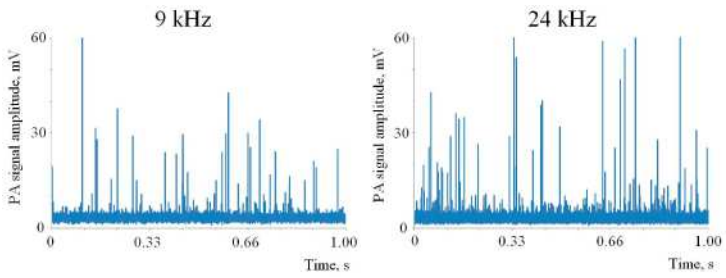

Fig. 6. PA detection of CNTs in a 350-μm tube *in vitro* at f_{rep} of 9 kHz and 24 kHz. Linear flow velocity, 2.5 m/s. Laser pulse energy, 30 μJ; excitation beam configuration in tube, 25×150 μm.

3.4 PA spectroscopy of biological tissues near 1064 nm in an animal model

Background light absorption of skin and blood and corresponding background PA signals can hide PA signals from circulating nanoparticles and cells. For lasers operating at 1064 nm, background signals are mostly associated with light absorption of water and oxyhemoglobin [Fig. 7(a)]. To estimate background signal in PAFC PA spectra from mouse blood vessel and nearby skin in the abdominal area were obtained. Figure 7(b) shows that the PA signal amplitudes from skin with blood vessel are of the similar amplitude at 1064 nm as signals acquired in 850–900 nm range. Typically used in most PA studies is the 650-900 nm range [3, 21]. The signal levels from skin at 1064 nm were ~4-fold less than those from a blood vessel. Thus, a laser operating at 1064 nm is an excellent optical source for PAFC providing low background signal from tissue components. It is possible to expect similar contrast between absorbing objects to that of a laser at 850–900 nm if objects' absorption spectra are similar in both spectral ranges, as is the case of CNTs or melanoma cells [8, 24].

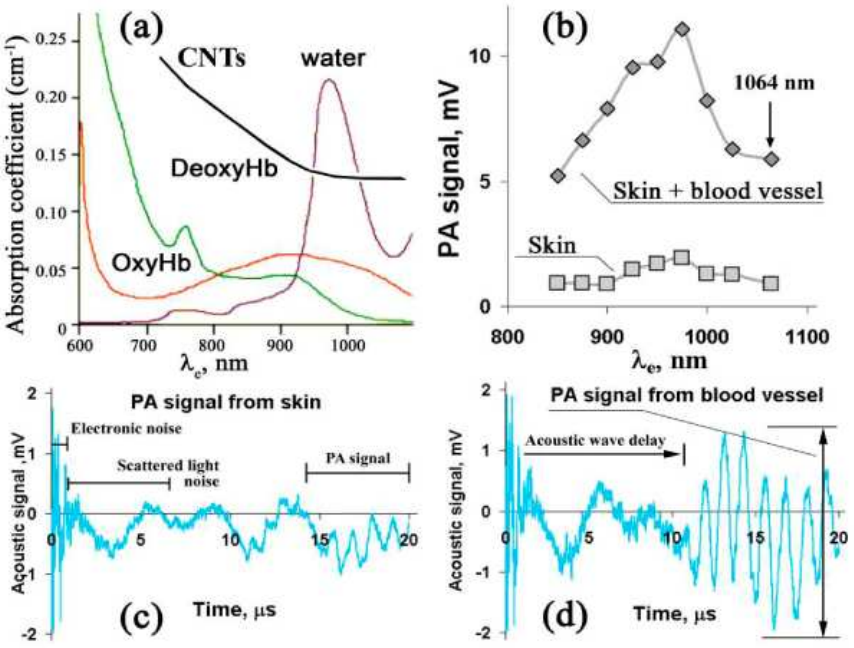

Fig. 7. Spectral characteristics of living tissue components and CNTs in the near-infrared region. (a) Light-absorption spectra of water [25], blood [26], and CNTs, 0.1 mg/mL solution in water; (b) PA spectra of skin with large blood vessels and of skin whitout it; (c,d) temporal shapes of PA signals from skin (c) and skin with blood vessels (d) measured at 1064 nm.

#122154 - $15.00 USD Received 5 Jan 2010; revised 3 Mar 2010; accepted 29 Mar 2010; published 9 Apr 2010

3.5 In vivo PA detection of circulating CNTs in an animal model

To estimate the capability of high-speed PAFC *in vivo,* 5 and 50-μL of 2.2 mg/mL CNTs solution were intravenously injected into tail veins of mice, and PA monitoring of 50–70-μm blood microvessels in the mouse ear followed. A linear laser beam of 20×100 μm focused on the mouse ear was enough to overlap an entire blood vessel (Fig. 8). Control monitoring of PA signals from blood vessels for 10–20 min before the injection revealed no false-positive signals at the selected level (3σ-criterion). The absence of PA signals in the control study was used as a proof that PA signals appearing after the injection of CNTs could be associated with circulating CNTs crossing the laser beam (Fig. 9).

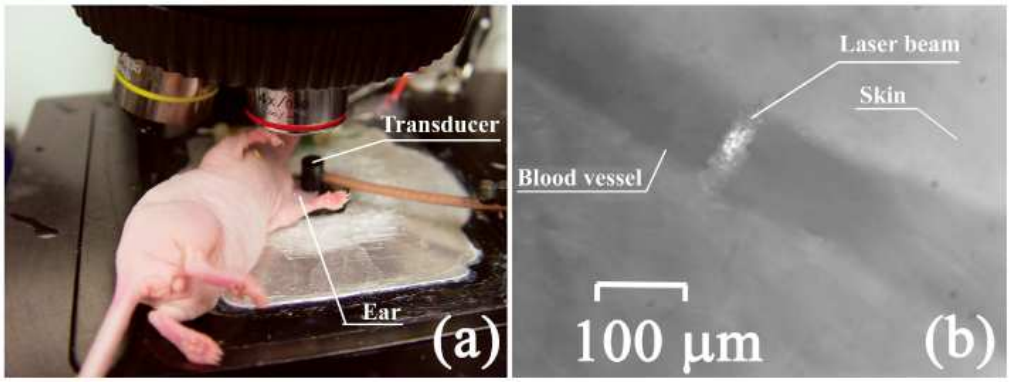

Fig. 8. *In vivo* PAFC. (a) Mouse on the microscopic stage; (b) photo of ear blood vessel and laser beam spot made in transmission mode by CCD camera.

The traces (Fig. 9) shows both an increase in the baseline level that we attribute to the presence of individual CNTs in the detection volume and strong fluctuations above of baseline associated with CNT aggregates. The clearance rate of CNTs was in the range of 20–30 min, although rare signals were seen over a few hours of observation. The experimental trace [Fig. 9(b)] was analyzed to verify the application of standard statistical analysis toward PAFC data. For each individual peak of the trace, the following parameters were calculated: position, width, and amplitude (height) [Fig. 2(d)]. These parameters were represented as histograms [Fig. 10(a)–10(c)] Their statistical distribution allows us to speculate about the pharmacokinetics of CNTs, the presence of aggregates (through the mean peak-width value), and size distribution (through peak-amplitude distribution).

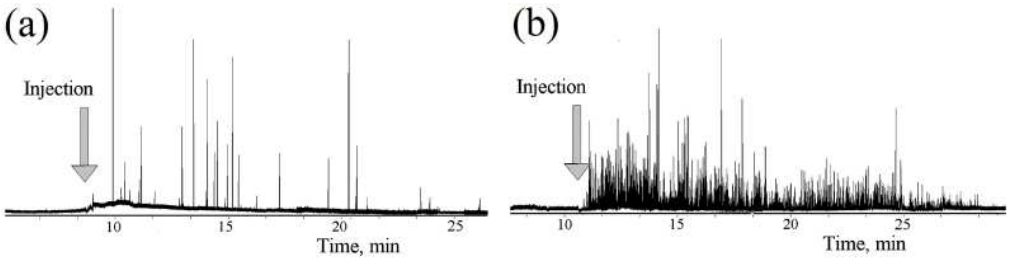

Fig. 9. Traces of PA signals from circulating CNTs in mouse blood: (a,b) Two experiments with different mice. Injection of 5 and 50-μL CNTs solutions in PBS. Conditions of experiment: f_{rep}, 9 kHz; laser pulse energy, 30 μJ; laser beam shape, 20×100 μm.

#122154 - $15.00 USD Received 5 Jan 2010; revised 3 Mar 2010; accepted 29 Mar 2010; published 9 Apr 2010

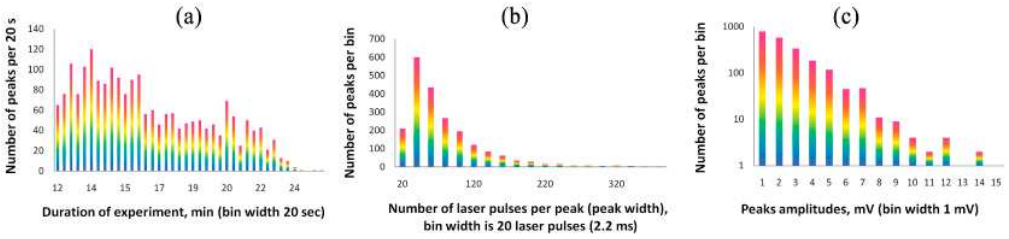

Fig. 10. Statistical analysis of *in vivo* PAFC data. (a) Histogram representing the rates of peak emergence during the experiment; bin width is 20 s; (b) distribution of peak widths; (c) histogram representing the distribution of peak amplitudes (in logarithmic scale). The histograms were calculated for the experimental data displayed in Fig. 9(b).

4. Discussion

4.1 The 1064 nm nanosecond laser for PAFC and other PA application

Lasers with wavelengths > 950 nm are not widely used for *in vivo* PA imaging and PAFC [3] or used with low pulse rate [28, 29]. However, if one compares near-infrared lasers having high PRRs, a short pulse duration, a pulse energy level up to 50–100 μJ, and a suitable cost, the choice of lasers operating in the window of transparency of biological tissues (650–930 nm) is limited, compared to the choice of well established laser systems operating at 1064 nm. Our results may be persuasive for broader application of 1064-nm lasers, especially with high PRRs. PA signal amplitudes from blood vessels obtained at 1064 nm are identical to those acquired at 850–900 nm [Fig. 7(b)]. The same was observed for background signal from skin only (i.e., without visible blood vessels, although we cannot exclude the presence of small capillaries). Thus, there was no significant increase in background signals of tissue components at 1064 nm. This finding opens the prospect of being able to select comparatively cheap and reliable laser sources operating at 1064 nm for the further development of the PA technique for flow cytometry, imaging, and microscopy.

Some potential, but not significant, drawbacks of this choice, from the viewpoint of sensitivity, are related to the limited number of PA contrast agents with absorption in this spectral range, such as melanin, CNTs, gold nanoshells, gold nanorods, and some other gold nanoparticles with different shapes and compositions. Further, light absorption by some nanoparticles at 1064 nm is 20–30% lower than at 650–900 nm. Taking into account a 10–20% increase in background signal from blood and skin, we expect total decrease in sensitivity at the level ~50% at 1064 nm compared to 850 nm. This situation, however, is improved due to the following: (1) the greater stability of more efficient laser sources operating at 1064 nm which may increase the accuracy of PT/PA measurements; (2) higher PRRs allowing increasing either the signal-to-noise ratio by 10–30-fold or the speed of PA analysis or imaging; and (3) an increase in the laser energy for *in vivo* measurement, as the laser fluence safety level at 1064 nm is 100 mJ/cm^2 compared to 20 mJ/cm^2 in the visible spectral range [30].

Figure 7(c), 7(d) illustrate some sources of noise to be considered in PAFC signal processing. Electronic noise (oscillations above 7 MHz level) with a typical duration of 1–2 μs is caused by the electromagnetic field generated by laser sources. Scattered laser light generates acoustic oscillations at the surface of the transducer that start right after the laser pulse. The moment when they appear does not depend on the distance from laser spot to transducer. With the transducer positioned at 4–6-mm distance from the laser beam, it takes 2–4 μs for acoustic waves generated by cells or nanoparticles to reach the transducer. We applied time-gating to select appropriate PA signals from the sample in time domain; thus, effects caused by both the electromagnetic field and scattered light were not recorded. Further digital bandpass filtration removes remaining noise and signal fluctuations. Standard

#122154 - $15.00 USD Received 5 Jan 2010; revised 3 Mar 2010; accepted 29 Mar 2010; published 9 Apr 2010

deviation of the PA signal amplitudes recorded for the blood sample decreased 3-fold with the use of digital filtration.

4.2 PT and PA effects at high laser pulse repetition rates

At high PRRs, many signals are acquired from each cell or nanoparticle crossing the laser beam. In this case, one could expect heat accumulation by medium or nanoparticles that could affect generation of PA signals. Typically, there are two kinds of samples in PAFC: (a) bulk tissue, blood vessels, individual cells or (b) nanoparticles of interests in tissue and blood. Depending on the sample size, laser beam spot, laser pulse energy, and PRR, PA signal generation could be efficient for cells but not for blood, or vice versa. Heat accumulation can decrease efficacy of PA signal generation or cause formation of strong PA signals by the generation of nano- and microbubbles.

To distinguish between equilibrium and heat accumulation, one needs to consider heat diffusion in the sample. In PT-based methods, the efficacy of laser energy conversion into thermal effects is maximal in the case of negligible heat diffusion from the sample into the surrounding medium as determined by thermal confinement $t_P \le \tau_T$ (where t_P is the laser pulse width and τ_T is the thermal relaxation time) [1,3]. For a spherical configuration, $\tau_T = D^2/27k$, where D is the diameter of the target and k is the thermal diffusivity of the sample (1.4×10^{-7} m^2/s for water). For typical targets with sizes D in the range of 100 nm, 1 μm, 10 μm, and 100 μm (e.g., nanoparticles, organelles, cells, or bulk media with a 100-μm laser spot), the thermal relaxation time τ_T is ~3 ns, 0.3 μs, 30 μs, and 3 ms, respectively. Thus, for a single 10-ns laser pulse, thermal confinement is fulfilled for most large targets; and it is not fulfilled for very small nanoparticles. However, this does not take in account heat accumulation at high PRRs that may reduce the amplitude of PT effects. For successive laser pulses, we can introduce a PRR confinement defined as $f_{rep}^{max} \le 1/\tau_T$. For $f_{rep} < f_{rep}^{max}$, there is enough time for heat diffusion to remove heat from the target to surrounding medium before the next pulse comes. For the typical targets indicated above, f_{rep}^{max} was estimated as 300 MHz, 3 MHz, 30 kHz, and 300 Hz, respectively. For example, the 300 Hz estimated for bulk samples corresponds well with the optimal frequencies used in PT thermal-lens spectroscopy method [2].

Flow in the vessel partly eases off thermal confinement as it removes excess heat from the laser spot and target [2]. This may decrease possible laser damage of the tissues and facilitate fulfillment of PRR confinement. For a flowing sample, the lifespan of target is defined as $\tau_f = D_L/v_f$, where D_L is the laser beam size along blood vessel and v_f is the linear flow velocity. For $\tau_f < \tau_T$, f_{rep}^{max} could be estimated as $f_{rep}^{max} \le 1/\tau_f$. For example, with a flow velocity v_f ~50 cm/s (large artery), the laser beam width, D_L ~10 μm and cell of 10 μm in the diameter, f_{rep}^{max} can be increased to 50 kHz compared to 10 kHz in static condition. For larger targets, the benefits in speed would be higher.

In photoacoustics, an efficient PA effect can be observed under fulfillment of the acoustic confinement defined as $t_P \le \tau_A = D/c_s$, where τ_A is the travel time for an acoustic wave through a target with diameter of D and c_s is the speed of sound in the medium (for water $c_s = 1.5\times10^5$ cm/s). For 100-nm and 10-μm targets, τ_A are 10 ns and 100 ps, respectively. Thus, a nanosecond laser that is effective in the PA detection of single cells might be less effective in the case of nanoparticle detection. However, our previous and current data demonstrate excellent PA sensitivity for small nanoparticles [5–7]. We hypothesize that, probably, fast temperature increases in nanoparticles due to fast non-radiative relaxation at the picoseconds time scale [31] may efficiently generate PA oscillations. Or acoustic confinement, like thermal confinement, is not important for nonlinear mode with fast nanobubble expansion that generates strong thermal [31] and acoustic phenomena, even with nanosecond pulses.

Overlapping of acoustic waves should limit f_{rep}^{max}. In the presence of acoustic reflections, the recorded acoustic response would be formed by a train of oscillations whose duration, τ_{TR}, is determined by transducer and setup parameters. With a τ_{TR} of ~5–15 μs, a PRR at f_{rep}^{max}

#122154 - $15.00 USD Received 5 Jan 2010; revised 3 Mar 2010; accepted 29 Mar 2010; published 9 Apr 2010

$<1/\tau_{TR}$ should be <200 kHz and ~60 kHz, respectively. Minimization of acoustic reflections and optimization of transducer response could decrease τ_{TR} to the 10-ns or 1-μs level, which could allow using f_{rep}^{max} at the levels of 100 MHz and 1 MHz, respectively. Moreover, overlapping of successive PA signals [Fig. 3(d)] could be used to enhance PA signals by fitting appropriate "resonant" PRR [1]. Indeed, we observed summation of individual oscillations at a f_{rep} of 420-kHz providing a 2–4-fold increase in signal amplitude [Fig. 3(a)].

Thus, for generation of acoustic signals from nanoparticles in linear mode, we considered five confinements: thermal, acoustic, flow escape time, and overlapping of thermal and acoustic waves. Under f_{rep} greater than f_{rep}^{max} calculated according to these confinements, linear PA signals from the sample would be degraded.

To verify these assumptions, we tested a solution containing 1-μm CNT aggregates in static conditions at a high f_{rep}. Above, we predicted that for f_{rep} values up to 3 MHz, there will be no effect of heat accumulation in the linear mode. PA signals observed experimentally were in a good correlation with our estimations: at a 1.0-μJ laser pulse energy level, local heat generation was not enough to generate even nanobubbles; only linear effects were observed [Fig. 3(a)]. The shape of the PT thermal-lens signals acquired from the sample prove this assumption [Fig. 3(b)]. In this mode, PA signal amplitude was almost constant up to f_{rep} = 0.5 MHz. Formation of stationary PT thermal-lens signals observed [Fig. 3(c)] indicates heat accumulation in the solution. At a higher laser pulse energy of 2 μJ [Fig. 3(a)], we observed effective bubble generation, though there was no sample decomposition or solution boiling until f_{rep} = 50 kHz. The average laser power at high PRRs heated the solution, simplified bubble generation, and led to increases in observed PA signal amplitudes. Nano- and microbubbles generation in this mode was proved by time-resolved PT thermal-lens techniques [Fig. 3(b)].

Given the model above, we may speculate that PAFC at high PRRs would benefit from thermal confinement observed for light-absorbing media, such as blood (heat accumulation would decrease linear background signal of blood), while PA effect from a small cell or a nanoparticle would not be degraded. This may increase PA contrast of small targets (e.g. individual nanoparticles) in the presence of blood cells or other light absorbing substances. The effects of nanobubbles formation from localized overheating or of acoustic signal overlapping could be used to further enhance signals from small targets passing the detection zone. We believe that temporal overlapping mode, with an optimized f_{rep}, could be combined with spatial overlapping mode [27] by selecting the laser energy level and nanoparticle parameters, including size, concentration, and spatial distribution. According to our calculations, these combined modes can amplify PA signals up to 10–50 times. We also propose the use of a high-PRR laser to generate periodic, relatively stable nano- and microbubbles around nanoparticle clusters to enhance both PA and PT diagnostic techniques and PT therapy of cancer and infections.

4.3 In vitro and in vivo assessment of PAFC

As we demonstrated [Fig. 5(b)], PAFC makes it possible to count nanoparticles in flow. With thick vessels or tubes, nanoparticles and cells flowing far from the irradiated zone would be missed, and an estimation of their numbers would be inaccurate. To avoid this, we implemented a cylindrical lens (an approach previously reported in [8]) to shape the laser beam into a linear strip. In this case, peak counts and peak widths are linearly dependent on the CNT concentration and the f_{rep}, respectively [Fig. 5(b), 5(c)]. Our experimental data have proven that this setup can operate at very high linear flow velocities up to 2.5 m/s. Along with peak count, there is a need to measure cell or particle velocity in flow. Conventional PA methods measure flow rate, but not the velocity, of a individual single cell or nanoparticle clusters [4,8,32]. Our data demonstrate that peak width corresponds well with the nanoparticle lifetime in the laser spot. For a certain f_{rep} and known laser spot size, D_L, linear

#122154 - $15.00 USD Received 5 Jan 2010; revised 3 Mar 2010; accepted 29 Mar 2010; published 9 Apr 2010

velocity v_{target} of a cell or nanoparticle could be estimated from the measured peak width, Δt, as $v_{target} = D_L/\Delta t$.

At a high f_{rep}, it is possible to increase detection sensitivity by averaging amplitudes of PA signals, which leads to a reduction of random noise. For example, if a CNT aggregate is exposed to five laser pulses at 5 kHz [Figs. 2(b), 2(c), and 7(b)], then at a f_{rep} of 100 kHz the same aggregate would be irradiated by 100 pulses. Thus, with data smoothing by moving the average filter, the background noise is decreased by $\sqrt{N}$ times, where N is the period of filtration (size of the averaged data subset) [1]. For a 10-point subset, there is a $\sqrt{10} = 3.1$ times decrease in random noise. Peak amplitude remains the same if peak width is larger than N. Averaging of the *in vitro* results proved this prediction, with the ratio between peak amplitude and background signal fluctuation increasing according to $\sqrt{N}$ law. The correlation coefficient for the linear curve describing the ratio between peak amplitude and standard deviation of the background signal (signal-to-noise ratio) at different PRRs is 0.98.

In general, one could expect two types of signals from nanoparticles in the laser beam, depending on the presence and the size of nanoparticle aggregates [Fig. 9(b)]. Individual nanoparticles, evenly spread in the medium, would act as a molecular solution and slightly increase the PA response of the sample. Significant-size aggregates would absorb laser radiation locally, thus providing a dramatic increase in the amplitude of PA signal.

The clearance kinetics of CNTs can easily be estimated from the distribution of peaks in the time after injection [Fig. 10(a)] as the rate of CNTs detection significantly decreases after 15-20 minutes. High-amplitude PA signals disappear from the traces recorded first [Fig. 9(a) and 9(b)]; so 15 min after injection there are only small CNTs in circulatory, that can be associated with clearance of large aggregates [Fig. 9(b)]. For each object passing through a laser beam, we can determine several parameters, such as peak amplitude and width [Figs. 2(c) and 10(a)–10(c)]. Given a known size distribution of injected particles (which is not the case with the CNTs used in this study), the distribution of peak widths [Fig. 10(c)] could be used to speculate about the flow velocity and aggregate formation in flow.

Acknowledgments

This work was supported in part by the National Institute of Health grant nos R01EB000873, R01CA131164, R01EB009230, and R21CA139373, the National Science Foundation grant nos DBI-0852737 and the Arkansas Biosciences Institute. We also thank the Office of Grants and Scientific Publications at UAMS for editorial assistance in the preparation of the manuscript.

#122154 - $15.00 USD Received 5 Jan 2010; revised 3 Mar 2010; accepted 29 Mar 2010; published 9 Apr 2010